Seismic tomography in boreholes

George A. McMechan *Department of Computer Science, University of Victoria, PO Box 1700, Victoria, BC V8W 2Y2, Canada*

Summary. Synthetic seismic tomographic data sets for cross-hole and hole-to-surface arrays are computed and inverted. Inversion (imaging) is performed through an iterative projection solution to a matrix equation. The orientation as well as the position of an anomaly relative to the source and recorder arrays affects both the rate of convergence of the solution and the resolution obtained. Data density and distribution determine the physical validity of the image obtained at convergence. Borehole tomography is apparently a viable method for imaging inter-hole structure.

Introduction

Tomography involves production of an image of a medium from data that are line integrals of the parameter to be imaged. Tomographic methods are widely applied in nuclear medicine (*cf.* Cormack 1973; Scudder 1978; Gullberg 1979) and in radio astronomy (*cf.* Bracewell & Riddle 1967) but have only recently been considered in applied geophysics. In view of the apparent success of tomography in the imaging problems to which it has been applied, further investigation in the context of seismic applications seems warranted.

Some geophysical tomography has been done. For example, the three-dimensional inversions for crustal and upper mantle velocity structure by Aki, Christofferson & Husebye (1977) and Spencer & Gubbins (1980) are a type of seismic tomography applied to refraction data; Kjartansson (1979) applies tomography to seismic reflection data; Lager & Lytle (1977) and Dines & Lytle (1981) apply it to electromagnetic data; Dines & Lytle (1979) apply it to both cross-hole electromagnetic and seismic data; Mason (1981) applies it to cross-tunnel seismic data.

The purpose of the present paper is the study of the characteristics of tomographic images, using the algebraic reconstruction technique (ART), of selected synthetic seismic examples in three geometrical configurations; cross-hole, hole-to-surface and the combination of these two.

Theory

The datum for seismic tomographic imaging is the integral of some physical parameter along a specified path through the medium. For example, the travel time accumulated along a ray

21

path between a source and a receiver can be expressed as the integrated slowness; the amplitude can be expressed as the integrated attenuation. All the examples below use travel-time observations that are imaged to determine a velocity distribution, but the method is completely general; any observation that can be defined as a line integral through the medium can be substituted throughout.

Two two-dimensional source to receiver configurations involving boreholes (cross-hole and hole-to-surface) are chosen as examples; these are geometrically simple but the methods described are applicable to any desired ray paths (Horn 1978). Fig. 1(a) shows a typical cross-hole configuration. Sources (S) are excited sequentially in borehole 1 and recorded on a string of recorders (R) in borehole 2. Each S is recorded at each R to provide a dense sampling of the medium between the holes. Because of the reciprocity of sources and recorders with respect to travel time, nothing is gained by interchanging the S and R positions. Similarly, Fig. 1(b) illustrates the hole-to-surface configuration; a similar
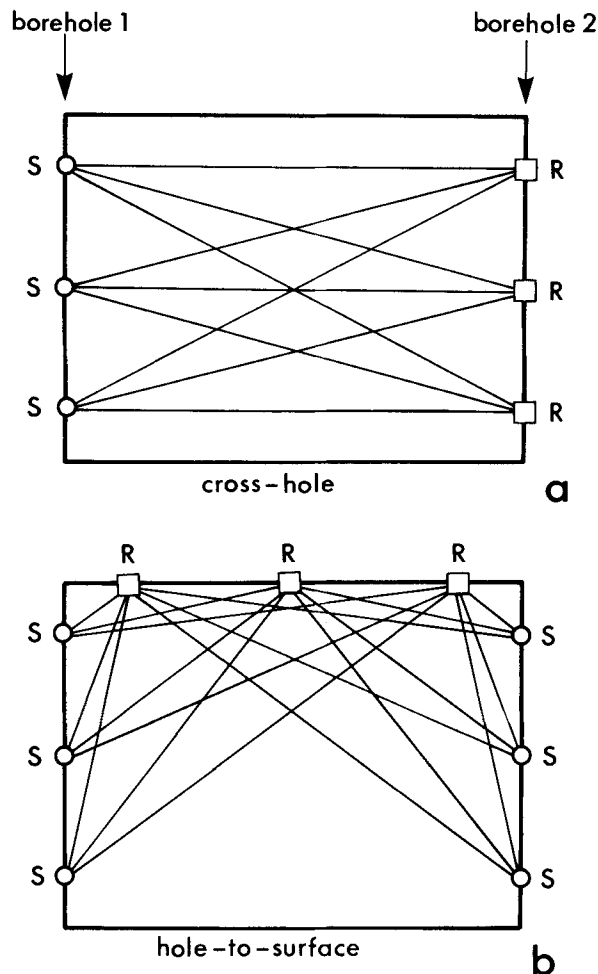
Figure 1. Borehole tomographic arrays. The upper (a) part of the figure shows the cross-hole configuration; the lower (b) part shows the hole-to-surface configuration. The left and right edges of each are boreholes; the material to be imaged lies in the vertical plane containing the holes. Source locations (S) and recorders (R) are joined by ray paths (the light solid lines).

geometry has been used by Newman & Worthington (1982) for attenuation measurements. In the examples below, the number of S locations in a borehole is 35; the number of R locations in a borehole is 35; the number of R locations on the surface is 50.

Because the medium is assumed to contain only small velocity variations all ray paths are approximated by straight lines. This approximation is made only for convenience and is not a critical part of the method. The straight ray assumption is realistic for disseminated (e.g. porphory) ore deposits in relatively homogeneous host rock and for any other media in which the local velocity variations are on a scale less than a wavelength of the source. The only modification required to allow for refractions associated with larger velocity variations is that the ray trajectories would have to be recomputed at each iteration rather than remaining fixed.

The region between boreholes is discretized into square boxes of dimension 0.018 × 0.018 km within which the properties of the medium are assumed to be constant. There are 35 boxes vertically and 50 horizontally in each of the models presented in the next section. This representation of the medium is arbitrary but very flexible; any desired model can be well approximated by using it.

Before dealing with tomographic imaging, consider the simpler problem of forward modelling. Modelling can be used independently as a method of data analysis by computing synthetic observations to compare with the real data but this approach, while instructive, is less efficient than direct ART inversion. In the present context, forward modelling is used to generate synthetic data for specified media to be used in evaluation of the inverse processing.

The notation used in both the forward and inverse problems is illustrated in Fig. 2. The medium in Fig. 2 consists of nine discrete square elements, the ith of which has constant slowness s_i (= velocity$_i^{-1}$). Consider the representative ray AB. This path consists of three segments; distance d_1 in slowness s_7, d_2 in s_4 and d_3 in s_1. The total travel time (TAB) for the ray AB is therefore:

$$TAB = d_1 s_7 + d_2 s_4 + d_3 s_1. \qquad (1)$$

A set of ray equations like (1) can be written in matrix form:

$$D s = T \qquad (2)$$
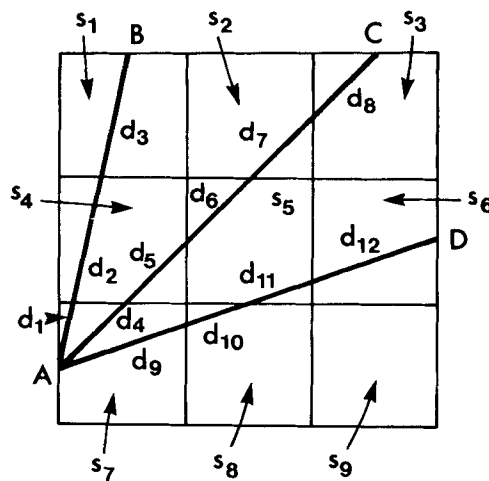
Figure 2. Definition of notation. An area to be imaged is divided into square elements. Within the ith element, the value (s_j) of the parameter to be imaged is constant. Ray paths (e.g. the heavy solid lines AB, AC and AD) are each composed of a series of segments (labelled d_j). Each ray segment traverses one model element.

where: D is an $N \times M$ matrix of distance increments d_j; M is the total number of slowness (or velocity) elements in the region between boreholes; N is the total number of rays; s is the slowness vector (length M); and, T is the vector of travel times (length N). For the three rays in Fig. 2, equation (2) is:

$$
\begin{bmatrix}
d_3 & 0 & 0 & d_2 & 0 & 0 & d_1 & 0 & 0 \\
0 & d_7 & d_8 & d_5 & d_6 & 0 & d_4 & 0 & 0 \\
0 & 0 & 0 & 0 & d_{11} & d_{12} & d_9 & d_{10} & 0
\end{bmatrix}
$$

$$
\times [s_1 \, s_2 \, s_3 \, s_4 \, s_5 \, s_6 \, s_7 \, s_8 \, s_9]^T = [\text{TAB TAC TAD}]^T \tag{3}
$$

where superscript T denotes transpose.

In performing the forward computations, D and s are known and the vector elements TXX are computed. In performing the inverse, D is known, TXX are observed and s is computed. M and N can be very large; in Figs 5(d) and 7(c), $M = 1750$ and $N = 4725$. Solutions for s by matrix operations on D (e.g. least squares) are therefore very consuming of both computer time and storage, and are also discouraged by the relatively sparse and random distribution of elements throughout D. An alternative is to solve for s with an iterative method that treats only one equation (one ray) at a time (*cf.* Gordon 1974). Examples are shown by Dines & Lytle (1979) and Herman, Lent & Rowland (1973) and a formal mathematical presentation is given by Tanabe (1971). Basically, the process of solving for s proceeds as follows:

(1) Make an initial guess for each element of vector s.

(2) Take the first ray (the first row of D) and multiply it by the current vector s to get a computed travel time T_c.

(3) Find the difference between T_c and the corresponding observed travel time (T_0) for the same ray.

(4) Adjust the value of each element of s that corresponds to a non-zero element in the current row of D so that $T_c - T_0 = 0$. There are a number of ways to do this (*cf.* Dines & Lytle 1979; Brooks & Di Chiro 1976) depending on how the time residual is distributed (or 'back projected') through the ray segments. For example, using the minimum energy criterion defines the correction in each segment to be proportional to the length of the segment.

(5) Repeat (2) to (4) for each ray (each row of D). Processing each row once constitutes one iteration. Iterations are performed until some convergence criterion is satisfied. The criterion in the present computer code is that the average absolute time residual be less than a specified amount.

The concept of convergence in the projection ART requires some discussion. If the rows of D are completely independent, the solution of equation (2) converges in one iteration (Tanabe 1971). Physically, this means that each box in the model is traversed by at most one ray. The resulting solution is non-unique because the integral time difference ($T_c - T_0$) constraint is independently met for each ray. It is possible to have complete convergence without a single correct slowness value since only the average slowness on each ray is constrained. These non-unique solutions depend primarily on the chosen starting model.

Another feature of projective solutions is evident when considering the unsampled box with slowness s_9 in the lower right corner of the model in Fig. 2. In equation (3), this box corresponds to the right-hand column of zeros in matrix D. The solution would never change the starting value of s_9. A slight smoothing applied between iterations would eliminate such

discontinuities in the image and increase the general stability of solutions for noisy data (Dines & Lytle 1979). The cost of smoothing is a small loss in resolution of detail.

In order to constrain the solution in a given box of the model, it is necessary to have > one ray passing through it; Crosson (1976) suggests a minimum of 10 for real data. In the synthetic examples presented below, every box in the grid is sampled a minimum of three times. Repeated sampling of the boxes makes the rows of D interdependent. The resulting projection inversion requires a number of iterations to converge; the slowness values at convergence are independent of the starting model. The reliability of these solutions is non-uniform over the model grid; it depends locally on the number of ray intersections within the region in question. For example, the cross-hole configuration (Fig. 1a) is most discriminating in the centre of the region between the boreholes; the hole-to-surface configuration (Fig. 1b) is most discriminating along the two sides and the top. Thus, these two configurations are expected to be complementary; the examples in the next section illustrate this.

Examples

This section illustrates the salient properties of seismic tomographic computations through a series of synthetic examples. Both forward modelling and ART inversions are included.

A representative cross-hole forward computation is contained in Fig. 3. Fig. 3(a) shows a velocity distribution between two boreholes. In this plot, and in most of the following ones, increasing velocity is represented by increasing the perceived darkness of the displayed pixels. Each individual pixel is produced by the superposition of up to five characters as specified in the 32-level grey scale of Henderson & Tanimoto (1974). Output is via a line printer.
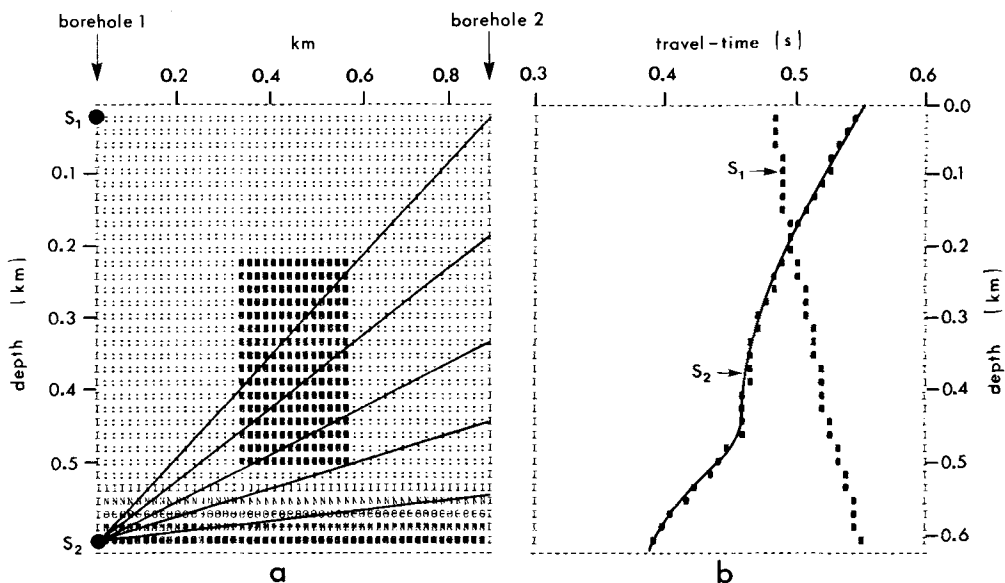
Figure 3. A representative synthetic forward problem. Tracing rays through the velocity distribution shown in (a) from sources S_1 and S_2 in borehole 1 (in a) to a string of recorders in borehole 2 produce travel-time curves S_1 and S_2 respectively (in b). Five representative rays from S_2 are shown as the solid lines in (a). The velocity in the rectangular region in the centre of (a) is 2.2 km s^{-1}; the velocity in the surrounding region is 1.8 km s^{-1}.

Two source locations in borehole 1 (S_1 and S_2) are considered in Fig. 3. Synthetic travel times for recording of source S_1 by a string of receivers in borehole 2 are labelled as line S_1 in Fig. 3(b). Similarly, the travel-time curve labelled S_2 (Fig. 3b) is for a source located at S_2 (Fig. 3a). Five representative rays from S_2 are superposed on Fig. 3(a) as the solid lines. A complete tomographic data set consists of the observations from all possible paths between the source and receiver arrays. For the present analyses internal reflections are not considered and are easily eliminated by including only first arrivals in the inversions.
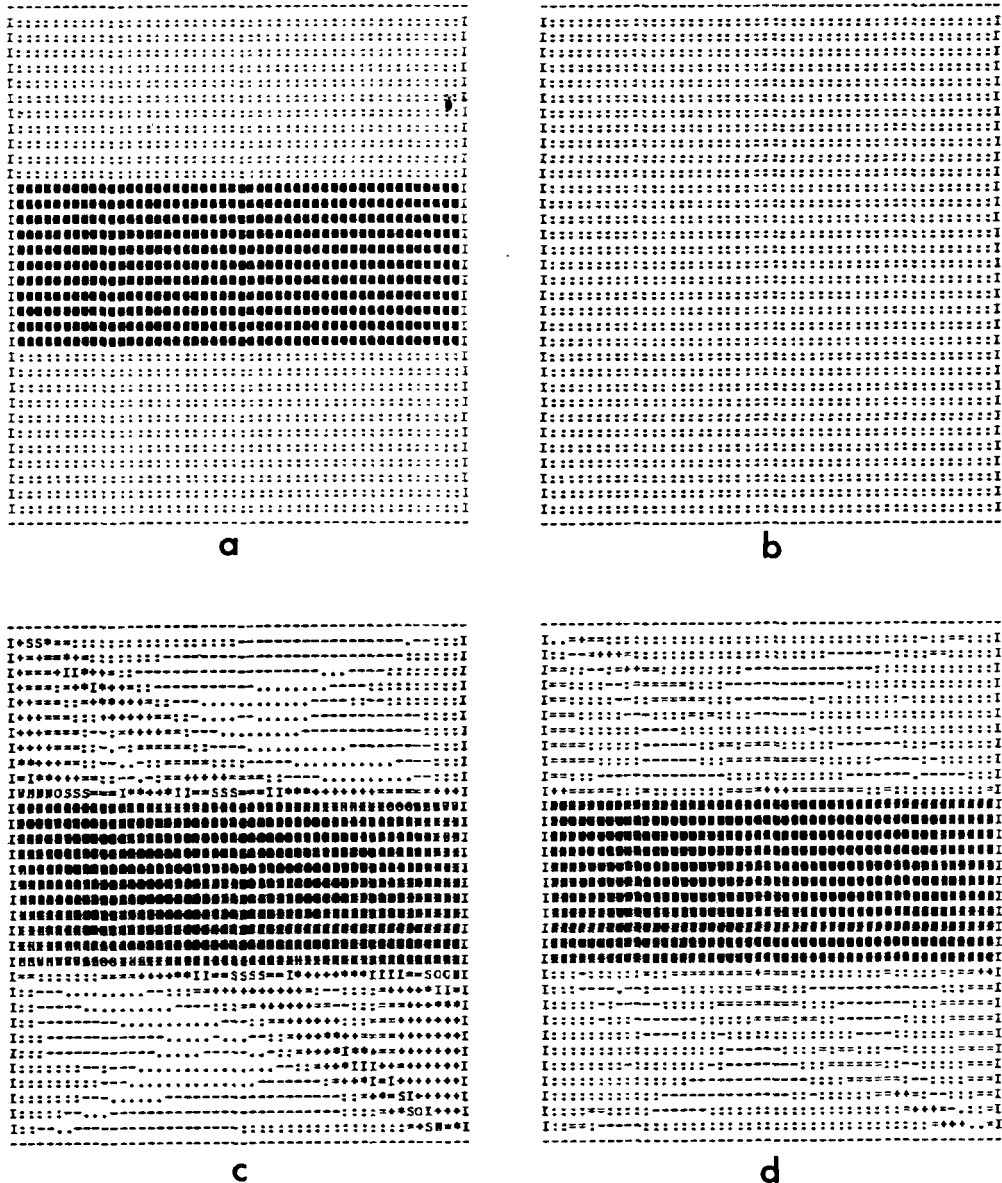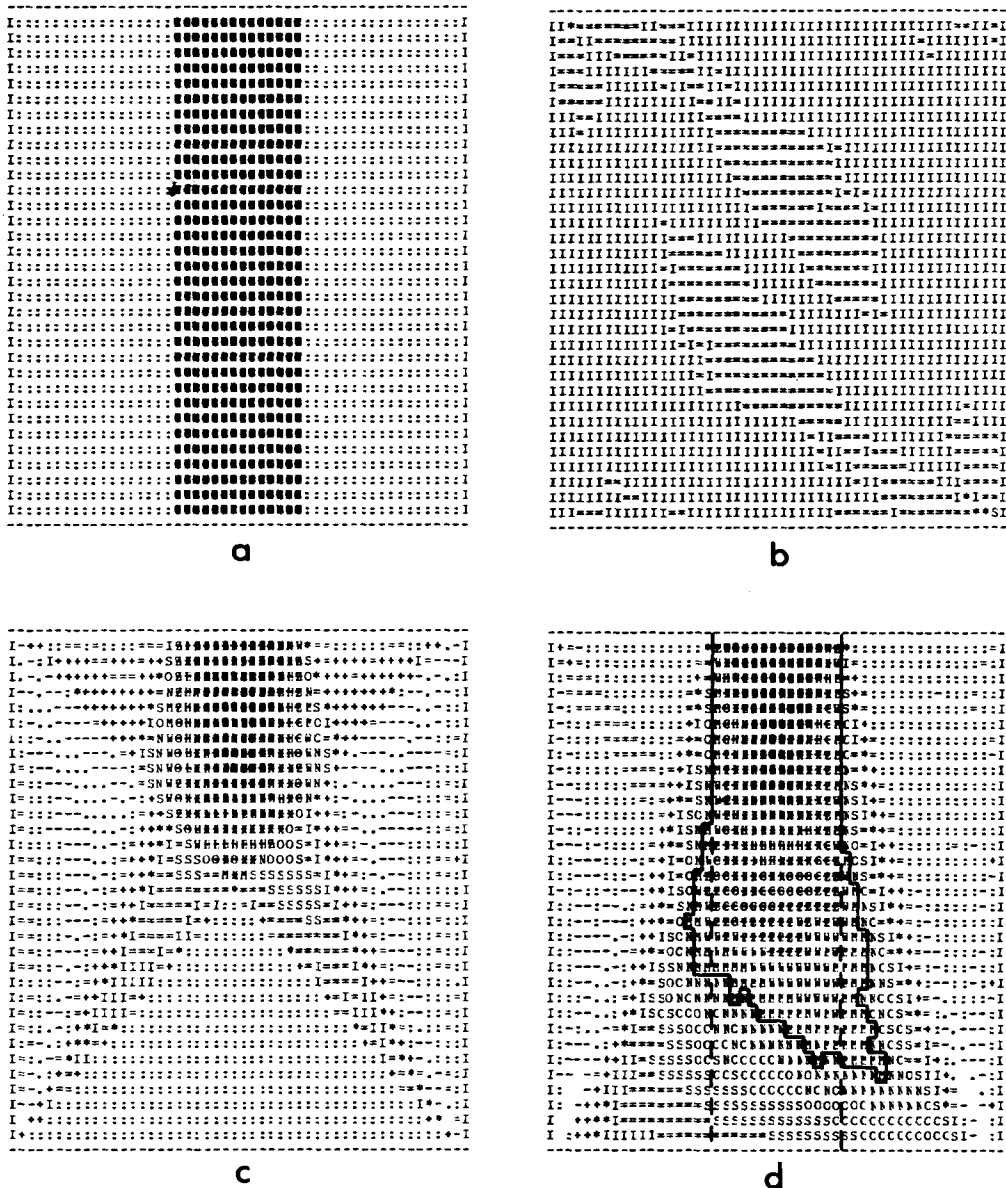

Figure 4. Tomographic imaging. Synthetic travel-time data computed for a cross-hole configuration for the model (a) are inverted using (b) as the starting model to give image (c) after two iterations and image (d) after 10 iterations.

The presentation of each of the following three synthetic examples (Figs 4, 5 and 7) follows the same pattern. In each, the (a) part of the figure shows the velocity distribution for the forward problem (which is also the correct or 'target' image for the inversion). A synthetic tomographic travel-time data set is computed for the model. Inversion of these synthetic data then proceeds iteratively, in each case using the constant velocity distribution

a

b

c

d

Figure 5. Tomographic imaging. Synthetic travel-time data computed for a cross-hole configuration for the model (a) are inverted using the starting model in Fig. 4(b) to produce image (b) after 10 iterations. Image (c) is the corresponding result for a hole-to-surface configuration. Image (d) is for combined cross-hole and hole-to-surface data; the area enclosed by the solid line (in d) shows the estimated extent of the vertical (dark) structure in (a) as determined at the 10th iteration. For comparison, the dashed lines indicate the actual boundaries of the structure.

of Fig. 4(b) as the common starting model. The remaining parts of the figures show various results. The image at 10 iterations is chosen arbitrarily as the basis for comparison of results among examples. For the present analysis and comparisons, these partially converged images are more revealing and instructive than their converged counterparts.

Fig. 4(a) shows a velocity distribution that is a simple, horizontally oriented high-velocity layer embedded in a lower velocity matrix. A synthetic cross-hole data set was generated for this model of 35 sources located at equally spaced positions down the left side and 35 receivers down the right side. Inversions of these data are shown in Fig. 4(b, c and d). Fig. 4(b) contains the (constant velocity) starting model used in inversion of this and all following examples. Fig. 4(c) is the result after two iterations and 4(d) is after 10. The result after two iterations is deceptively good. Both the shape and velocity contrast of the structure are well defined (compare with the correct solution in Fig. 4a). The main factor in the rapid convergence of this example is the orientation of the sampling rays (see the cross-hole configuration in Fig. 1a) relative to that of the anomalous structure. With all the sources on one side and all the recorders on the other, the ray paths have a dominant trend that parallels the structural boundaries. Since ART imaging is constrained to fit only the integrated slowness value along each ray path, resolution of the slowness in a region requires independent sampling of the region by many rays. However, in the present example, the target slowness value at any point is equal to the average value in the corresponding horizontal line. Thus, the point and integral criteria are functionally similar for this geometry and the convergence to the correct value at each point is as fast as convergence to the correct integral values. Fig. 4(d) shows that increasing the number of iterations progressively increases the imaging of details; the edges of the anomaly become more sharply defined and the absolute values of velocity in all regions of the image converge to the correct solution.

If the horizontal anomaly in Fig. 4(a) is optimally oriented to be imaged by a cross-hole array, then the vertical anomaly in Fig. 5(a) should be poorly resolved by the same array. This prediction is confirmed in Fig. 5(b) which shows the result of reconstruction of the model in Fig. 5(a) from synthetic cross-hole data. Compare Figs 4(d) and 5(b), which are both for 10 iterations using data from identical cross-hole arrays. The poor image in Fig. 5(b) is attributed to two effects that are both related to the fact that all rays necessarily pass through similar slowness regions. The first effect is that there is a high level of dependence in the columns of matrix D (equation 2) that results in slowed convergence. Secondly, it is almost as easy to satisfy the travel-time integral constraint with a smoothed slowness distribution as with one containing sharp transitions. In Fig. 5(b), there is a hint of a diffuse anomalous zone near the centre of the image, but its velocity values are too low; the values in the surrounding region are correspondingly high. However, the average velocity along any ray path is well fitted; in fact, the average time residual over all rays is smaller for Fig. 5(b) than for Fig. 4(d).

Further evidence for geometrical sensitivity is presented in Fig. 5(c). Fig. 5(c) contains the result of imaging a synthetic hole-to-surface (see configuration in Fig. 1b) data set for the model in Fig. 5(a). Ten iterations were done so a direct comparison can be made with Fig. 5(b). As expected, resolution is highest in the upper central part of the image where the rays are densest; the correct solution is stabilizing there.

Consider now a joint inversion of the combined cross-hole and hole-to-surface data for the model in Fig. 5(a). The result (again for 10 iterations to allow comparisons) is presented in Fig. 5(d). Here, the interaction of the two data sets produces an image that is better than that obtained by using either the cross-hole or the hole-to-surface data alone. In the correct solution (Fig. 5a), only two different velocities are present. Thus, a simple (arbitrary)

method for estimating the spatial distribution of the two materials at any iteration is to set a cut-off criterion that is the average of the two velocities; then, locations with velocities less than the average are assigned to one material and those with more, to the other. In Fig. 5(d), the criterion line so obtained is the solid line; the correct (target) boundary is the dashed line. As expected, the upper half of the image is relatively well converged because of the strong influence of the hole-to-surface data, with progressively poorer convergence with increasing depth. Complete convergence can of course be obtained by continuing the iterations (Fig. 4), but the converged image is of lesser value for the present analysis.

A most important feature of Fig. 5(d) is that convergence in the lower central part of the image is improved by adding hole-to-surface constraints even though the corresponding rays do not pass through this region. This apparent paradox is explained by referring to Fig. 6. If the time integral constraint is satisifed for ray AA′ independently of other rays, only the average slowness on path AA′ is constrained. If, however, rays 1–6 from source B are included to provide constraints on the upper part of AA′, then the average velocity computed for the remainder of AA′ (enclosed by the dashed line) becomes more tightly constrained through a reduction of the effective number of degrees of freedom. A ray therefore provides direct constraints in the region through which it passes, plus indirect constraints in all regions crossed by the rays that intersect it. Thus, as noted above, the image produced by combining cross-hole and hole-to-surface data is considerably better than that obtained from either separately because of their interactions.

As a final example, consider the model in Fig. 7(a). This model combines a number of features that have been treated individually in the foregoing examples. There is a rectangular, closed, high-velocity anomaly in the centre of the model and a linear increase in velocity as a function of depth near the bottom. The result of 10 iterations of cross-hole data alone is presented in Fig. 7(b). The starting model is shown in Fig. 4(b). For the rectangular region, the decision criterion (as defined above) is plotted as the solid line; the dashed line is the target solution. The image of the rectangle, particularly at its top and bottom edges, is beginning to emerge in the correct location, but it is still smoothed; velocities are too low in the rectangle and too high in the surrounding region.

Fig. 7(c) contains the result of inversion of combined cross-hole and hole-to-surface data. Although Fig. 7(b) and (c) are both for 10 iterations, (c) is a better image; the solid line [the current approximation to the target (dashed) rectangle] is a single closed area and the
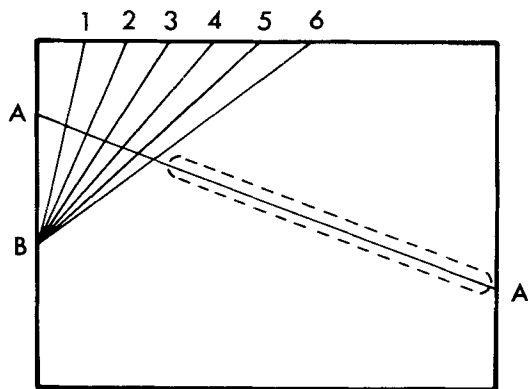

Figure 6. Indirect constraints. Rays 1–6 from source B indirectly constrain the solution in the region enclosed by the dashed line by providing direct constraints on the upper portion of ray path AA′.
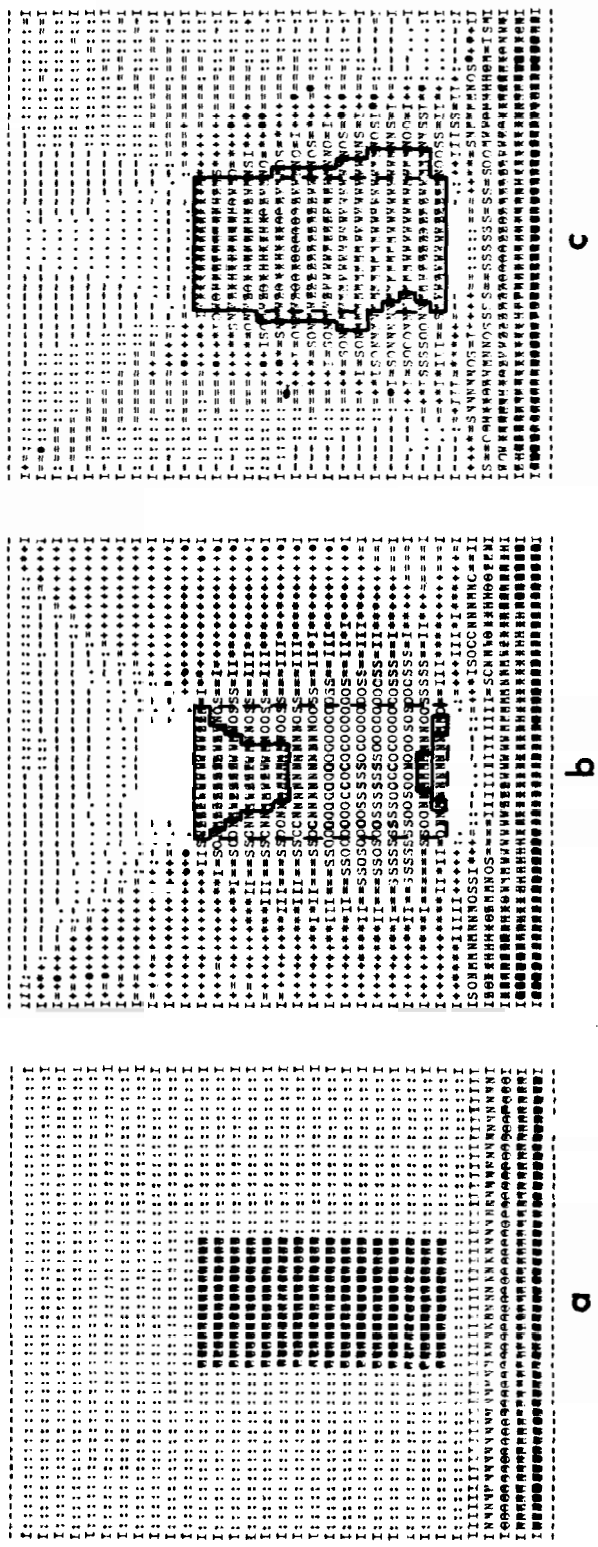
Figure 7. Tomographic imaging. Synthetic travel-time data computed for a cross-hole configuration for the model (a) produce the image (b) after 10 iterations from the starting model shown in Fig. 4(b). Similarly, imaging of combined cross-hole and hole-to-surface data produces image (c). In (b) and (c) the solid lines are the estimated boundaries of the rectangular anomaly in the centre of (a) after 10 iterations. The dashed lines are the correct (target) boundaries; (c) is clearly a better estimate than (b).

velocities are everywhere much closer to the target values as displayed in Fig. 7(a). In both Fig. 7(b) and (c), the position and extent of the horizontal features are, as predicted in Figs 4 and 5, well-defined relative to the vertical ones.

Discussion and synopsis

This study illustrates the characteristics of imaging tomographic seismic data by ART implemented through iterative projection. It is demonstrated through a series of synthetic examples that borehole configurations are viable for imaging inter-hole structures. The method is general and can be used with any arbitrary ray sampling scheme. For example, another application is in imaging structure between mine tunnels from underground recordings (*cf*. Mason, Buchanan & Booer 1980 and Mason 1981).

A number of further studies are suggested by the results obtained here. Since the same algorithm can be used for any parameter of the medium that can be expressed as a line integral, it should be possible to do joint inversion for a number of parameters simultaneously (e.g. a combination of seismic travel time, seismic amplitude and electromagnetic data). Another extension is suggested by noting that the data are essentially point observations; it should be possible to make use of the complete recorded wavefields. Also tomographic imaging is directly applicable to three- as well as two-dimensional seismic structures. Finally, tomography needs to be further evaluated in a practical sense by application to real data.

The computations involved in tomographic imaging by iterative projection are relatively straightforward. Their main characteristic is that they are highly repetitive vector operations; the method is therefore ideally suited to implementation in an array processor. Further numerical work on speeding convergence would also be a positive contribution, as would a dynamic grid specification that depends on the spatial distribution of detail and sampling density (Christofferson & Husebye 1979 have attempted this). Matrix D (equation 2), which is usually overdetermined, can become underdetermined as the number of grid elements increases. This raises the question of whether different inversion algorithms may be desirable for each. Projection can be used for solution of both but has the disadvantage for the over-determined condition that the solution after each iteration depends more strongly upon the most recently processed rows of D rather than being optimized over all the rays. This produces different rates of convergence in different parts of an image (see the asymmetry in the partially converged image in Fig. 5d).

In summary, tomographic processing is a viable means of imaging seismic structure between bore-holes.

Acknowledgments

References

Aki, K., Christofferson, A. & Husebye, E. S., 1977. Determination of the three-dimensional seismic structure of the lithosphere, *J. geophys. Res.*, **82**, 277–296.

Bracewell, R. N. & Riddle, A. C., 1967. Inversion of fan beam scans in radio astronomy, *Astrophys. J.*, 150, 427–434.

Brooks, R. A. & Di Chiro, G., 1976. Principles of computer assisted tomography (CAT) in radiographic and radioisotopic imaging, *Phys. Med. Biol.*, 21, 689–732.

Christofferson, A. & Husebye, E. S., 1979. On three-dimensional inversion of P wave time residuals: option for geological modeling, *J. geophys. Res.*, 84, 6168–6176.

Cormack, A. M., 1973. Reconstruction of densities from their projections with applications in radiological physics, *Phys. Med. Biol.*, 18, 195–207.

Crosson, R. S., 1976. Crustal structure modeling of earthquake data 1. Simultaneous least squares estimation of hypocenter and velocity parameters, *J. geophys. Res.*, 81, 3036–3046.

Dines, K. A. & Lytle, R. J., 1979. Computerized geophysical tomography, *Proc. IEEE*, 67, 1065–1073.

Dines, K. A. & Lytle, R. J., 1981. Analysis of electrical conductivity imaging, *Geophysics*, 46, 1025–1036.

Gordon, R., 1974. A tutorial on ART (Algebraic Reconstruction Technique), *IEEE Trans. Nucl. Sci.*, NS-21, 78–93.

Gullberg, G. T., 1979. The attenuated Radon transform: theory and application in medicine and biology, *PhD thesis*, Lawrence Berkeley Laboratory, University of California.

Henderson, P. & Tanimoto, S., 1974. *Considerations for Efficient Picture Output via Line Printer*, Report No. 153, Computer Science Laboratory, Electrical Engineering Department, Princeton University.

Herman, G. T., Lent, A. & Rowland, S., 1973. ART: Mathematics and applications: A report on the mathematical foundations and on the applicability to real data of the algebraic reconstruction techniques, *J. theor. Biol.*, 43, 1–32.

Horn, B. K. P., 1978. Density reconstruction using arbitrary ray sampling schemes, *Proc. IEEE*, 66, 551–562.

Kjartansson, E., 1979. Attenuation of seismic waves in rocks and applications in energy exploration, *PhD thesis*, Stanford University.

Lager, D. L. & Lytle, R. J., 1977. Determining a subsurface electromagnetic profile from high-frequency measurements by applying reconstruction technique algorithms, *Radio Sci.*, 12, 249–260.

Mason, I. M., 1981. Algebraic reconstruction of a two-dimensional velocity inhomogeneity in the High Hazles seam of Thoresy colliery, *Geophysics*, 46, 298–308.

Mason, I. M., Buchanan, D. J. & Booer, A. K., 1980. Channel wave mapping of coal seams in the United Kingdom, *Geophysics*, 45, 1131–1143.

Newman, P. J. & Worthington, M. H., 1982. In-situ investigation of seismic body wave attenuation in heterogeneous media, *Geophys. Prosp.*, 30, 377–400.

Scudder, H. J., 1978. Introduction to computer aided tomography, *Proc. IEEE*, 66, 628–637.

Spencer, C. & Gubbins, D., 1980. Travel-time inversion for simultaneous earthquake location and velocity structure determination in laterally varying media, *Geophys. J. R. astr. Soc.*, 63, 95–116.

Tanabe, K., 1971. Projection method for solving a singular system of linear equations and its applications, *Numer. Math.*, 17, 203–214.